Table S1 (Related to Figure 1). Overview of buried residues and hydrogen bonds at interaction interfaces

Buried residues in the IL-23:IL-23R:Nb22E11 structure listed per interface determined by PISA http://www.ebi.ac.uk/pdbe/pisa/

IL-23R:IL-23p19	
IL-23R	**IL-23p19**
Gly24	Asp55
Ile25	Leu56
Thr26	Arg57
N27	Glu58
Ile28	Glu59
N29	Gly60
Cys30	Asp67
Ser31	Val68
Ile56	His70
Lys57	Phe99
Tyr67	Tyr100
N69	Leu103
Gly70	Ile108
Ser98	Pro113
Met99	Q154
Tyr100	Pro155
Thr102	W156
His108	Q157
Phe109	Leu159
Q110	Leu160
Glu111	Leu161
Thr112	Lys164
Leu113	Ile165
Cys115	Arg167
Gly116	Ser168
Lys117	
Asp118	

IL-23R:IL-12p40	
IL23R	**IL-12p40**
Arg62	Lys107
Pro106	Asp109
Lys107	Gly110
His108	Ile111
Phe109	W112
Q110	Thr114
	Lys124
	Lys126
	Phe128
	Tyr223
	Thr224

IL-12p40: IL-23p19	
IL-12p40	**IL-23p19**
Lys124	Q34
Tyr136	Q38
Ala198	Cys41
Cys199	W45
Ala201	Asp55
Ala202	Pro69
Glu203	His70
Glu204	Ile71
Ser205	Q72
Phe228	Cys73
Arg230	Gly74
Pro265	Cys77
Ser267	Asp78
Tyr268	Pro79
Phe269	Leu82
Ser270	Tyr100
Asp292	Arg167
Asp312	Ser168
Arg313	Q170
Tyr314	Ala171
Tyr315	Phe172
Ser316	Ala174
	Val175
	Ala177
	Arg178
	Val179
	Ala181
	His182
	Ala185
	Thr186

IL-12p40:Nb22E11	
IL-12p40	**Nb22E11**
Leu35	Arg27
W37	Thr28
Pro39	Phe29
Asp40	Ser30
Leu62	W31
Asp63	Glu44
Glu67	Arg52
Lys80	Gly56
Glu81	Ser57
Phe82	Pro58
Gly83	Tyr59
Ala85	Lys65
Lys106	Ser100
Glu108	Leu101
Asp115	Phe102
Ile116	Pro103
Lys118	Thr104
Thr147	Ser105
Ile148	Arg106
Ser149	His109
N184	Asp111
His216	
Lys217	
Leu218	
Lys219	

Hydrogen-bonds in the IL-23:IL-23R:Nb22E11 structure listed per interface as determined by Chimera

IL-23R: IL-23p19		
IL-23R		**IL-23p19**
Gly24	-	Lys164
N27	-	Lys164
N29	-	Glu58
Glu111	-	Arg57
Thr112	-	Arg57
Leu113	-	Arg57
Asp118	-	W156

IL-23R: IL-12p40		
IL23R		**IL-12p40**
Arg62	-	Asp109
Arg62	-	Asp109

IL-12p40: IL-23p19		
IL-12p40		**IL-23p19**
Glu203	-	His70
Glu203	-	Ile71
Glu203	-	Ile71
Ser267	-	His182
Tyr268	-	Cys77
Asp292	-	Q38
Asp312	-	Arg178
Asp312	-	Arg178

IL-12B:Nb22E11		
IL-12p40		**Nb22E11**
Asp40	-	Lys65
Asp63	-	Arg106
Phe82	-	Pro103
Gly83	-	Arg106
Gly83	-	Arg106
Ala85	-	Arg106
Glu108	-	Arg52
Glu108	-	Arg52
Glu108	-	Arg52
N184	-	Thr28

Buried residues in the IL-23:Briakinumab^{Fab} structure listed per interface (only between p40 and Fab and observed at least twice) as determined by PISA

IL-12p40:Heavy	
IL-12p40	**Heavy**
Asp36	Q1
W37	Val2
Tyr38	Gly26
Pro39	Phe27
Asp40	Thr28
Ala41	Ser31
Lys80	Tyr32
Glu81	Gly33
Phe82	Arg52
Lys106	Tyr53
Lys107	Ser56
Glu108	N57
Asp109	Tyr59
Gly110	Thr98
Ile111	His99
Ser113	Gly100
Thr114	Ser101
Asp115	His102
Leu117	Asp103
Lys118	N104
Asp119	
Lys121	
Thr147	
Ile148	
Lys219	

IL-12p40:Light	
IL-12p40	**Light**
Asp36	N32
Tyr38	Thr33
Lys107	Lys35
Asp109	Tyr50
Gly110	Tyr51
Ile111	Q90
W112	Tyr92
Ser113	Arg94
Thr114	Tyr95
Lys124	Thr96
N125	His97
Lys126	Pro98
	Leu100

Hydrogen-bonds in the IL-23:Briakinumab^{Fab} structure listed per interface (only between IL-23 and Fab and observed at least twice) as determined by Chimera

IL-12p40:Heavy		
IL-12p40		**Heavy**
Asp36	-	Ser101
W37	-	Ser31
Asp109	-	Gly100
Lys219	-	Tyr53

IL-12p40:Light		
IL-12p40		**Light**
Asp36	-	Tyr51
Asp109	-	Lys35

Table S2 (Related to Figure1). Mapping of missense SNP onto the IL-23:IL-23R structure.
SS=Signal sequence; CP=Cytoplasm; TM=transmembrane domain; EC=Extracellular; D1=Domain 1; D2=Domain 2; D3=Domain 3.
Most common missense mutations in hIL-23R according to the Exome Aggregation Consortium (ExAC) browser (http://exac.broadinstitute.org). Highlighted residues are present in the IL-23:IL-23R:Nb22E11 structure reported herein.

Mutation	Rs number	Location	References/pathophysiology
L310P	7530511	D3	Duer et al. 2006 →GWAS →no effect on IBD Cargill et al. 2007 → SNP meta analysis → protective against psoriasis Huber et al. 2008 → targeted genotyping →susceptibility to Graves' Opthalmopathy
Q3H	1884444	SS	Duer et al. 2006 →GWAS →not linked to IBD Cargill et al. 2007 → SNP meta analysis → not linked to psoriasis Li et al. 2016 → targeted sequencing → susceptibility to MS
R381Q	11209026	CP	Duer et al.2006 →GWAS →protection against IBD Cargill et al. 2007 → SNP meta analysis → protective against psoriasis Huber et al. 2008 → targeted genotyping →not linked to Graves' Opthalmopathy Silverberg et al. 2009 → GWAS →protection against UC Pidasheva et al. 2011 → reduced surface expression and activation Momozawa et al. 2011 → targeted sequencing →protective against IBD Raymond et al. 2014 → soluble IL23R isoform Sivanessan et al. 2016 →reduced surface expression Peng et al. 2017→ GWAS meta analysis → protective against UC
V362I	41313262	TM	Rivas et al. 2011 → targeted sequencing → protective against IBD Momozawa et al. 2011 → targeted sequencing → protective against IBD Sivanessan et al. 2016→reduced surface expression →protective
G149R	76418789	D2	Rivas et al. 2011 → targeted sequencing → protective against IBD Momozawa et al. 2011 → targeted sequencing →protective against IBD Onodera et al. 2015 →targeted sequencing → protective against CD Sivanessan et al. 2016→ reduced surface expression
R86Q	76575803	D1	Momozawa et al. 2011 → targeted sequencing →protective against IBD
A199V	143130647	D2	
L193F	146440064	D2	
S559R		CP	
P306S	147093105	D3	
V160A		D2	
S221F		D3	
L372F		TM	
I373G		TM	
V159M		D2	
I341M		EC	
I354T		EC	
D129E		D2	

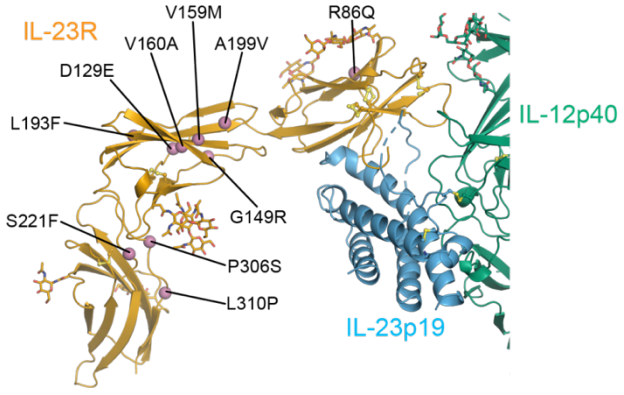

Most common missense mutations in human IL-12p40 according to the ExAC browser.

Mutation	Rs number	Location	References/pathophysiology
V298F	3213119	D3	Cargill et al. 2007 → no significant genetic association with psoriasis Prescott et al. 2015 → targeted sequencing → protective for IBD Fang et al. 2015 → SNP meta analysis → melanoma susceptibility
V33I	3213096	D1	Cargill et al. 2007 → no significant genetic association with psoriasis Fang et al. 2015 → SNP meta analysis → no effect on melanoma susceptibility
S226N	55661460	D2	
R288T	370904274	D3	
R250Q	74644143	D3	
G182R	10045130	D2	
E95K	562877471	D1	
T169M		D2	
V275I	189324104	D3	
T291M		D3	
R179T	375159171	D2	
S100L	144694601	D1	
E321K		D3	
V325M	56064925	D3	
L101F		D1	
V96F		D1	
E81G		D1	
G171R	189313574	D2	

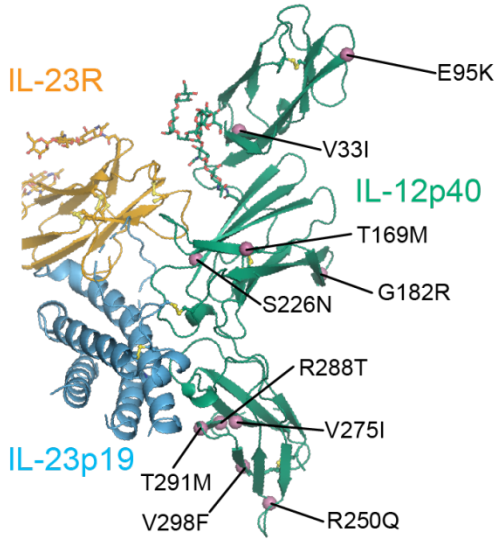

Most common missense mutations in human IL-23p19 according to the ExAC browser.

Mutation	Rs number	Location	References/pathophysiology
P14L	145233794	SS	
R178Q		αD	
M8I		SS	
L2P		SS	
S106L		αB	
P117L		BC loop	
A177T		αD	
R158C		αD	
P14T		SS	
R158H	146998334	αD	
P113A		BC loop	
P113L		BC loop	
T144S		CD loop	
K164R		αD	
E58Q		AB loop	

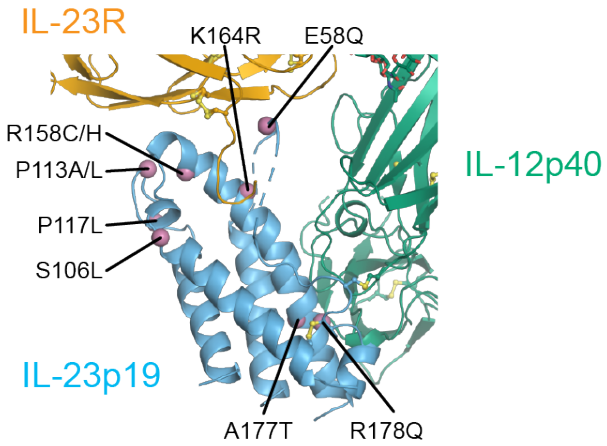

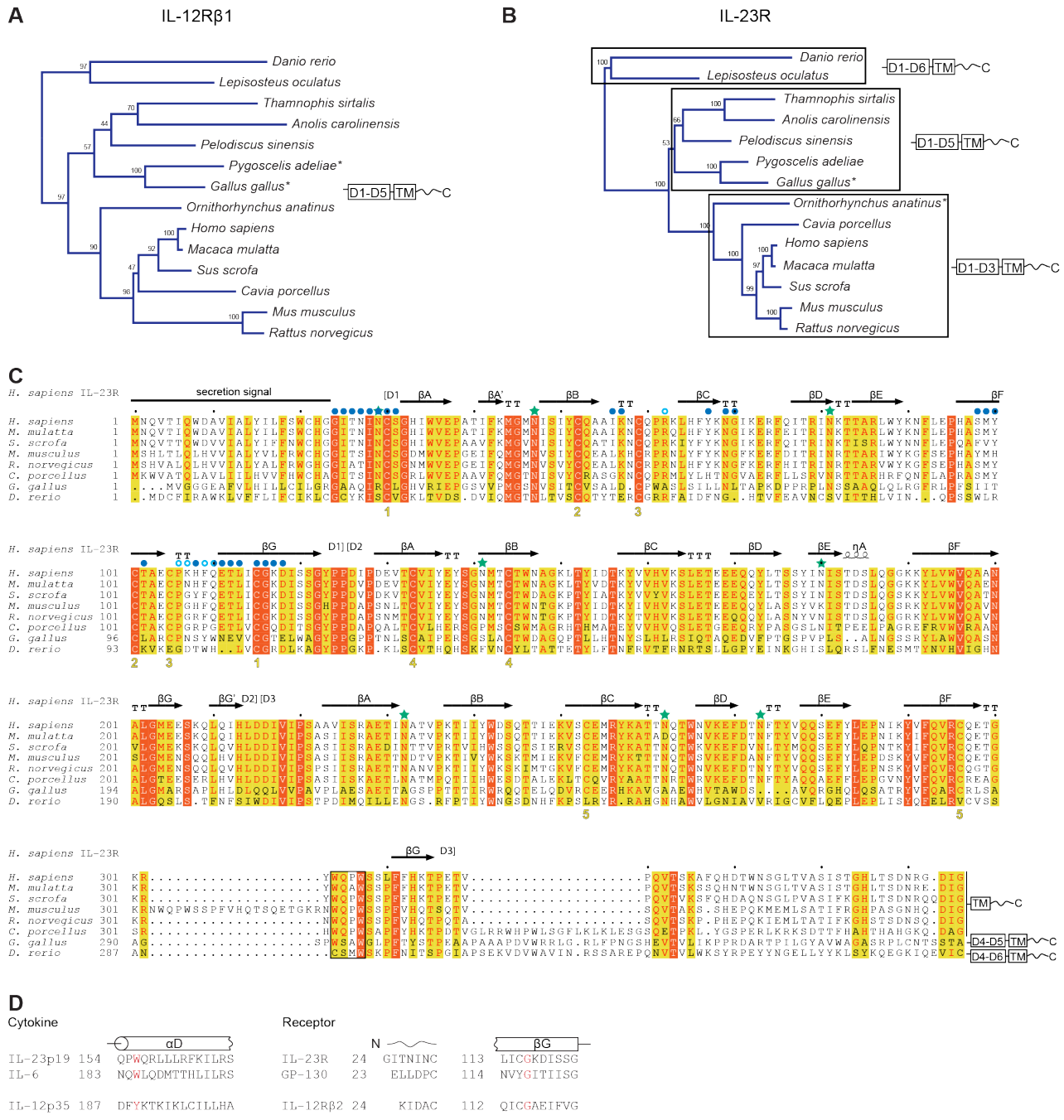

Figure S1 (Related to Figure 1). Phylogenetic analysis of IL-23R and sequence alignments.
Phylogenetic analysis of IL-12Rβ1 (**A**) and IL-23R (**B**). The mammalian IL-23R orthologues cluster distinctly from those in lower-jawed vertebrates, which have additional FnIII domains. Asterisks indicate sequences manually assembled from available genomic data. Multiple sequence alignments were performed with MAFFT 7 using the E-INS-I algorithm for refinement. The phylogenetic analysis was performed on the http://mafft.cbrc.jp/alignment/ server. (**C**) Structurally annotated multiple sequence alignments of the extracellular domains of IL-23R using the ESPripT server (http://espript.ibcp.fr/ESPript/ESPript/). Stars indicate N-linked glycosylation sites, full blue spheres residues interacting with IL-23p19, and hollow blue spheres residues interacting with IL12p40. The characteristic WSXW motif in the CHR region is indicated by a black box. (**D**) Structure-based sequence alignment of cytokine and receptor regions in IL-23:IL-23R and IL-6:gp130 complexes, IL-12p35, and IL-12Rβ2.

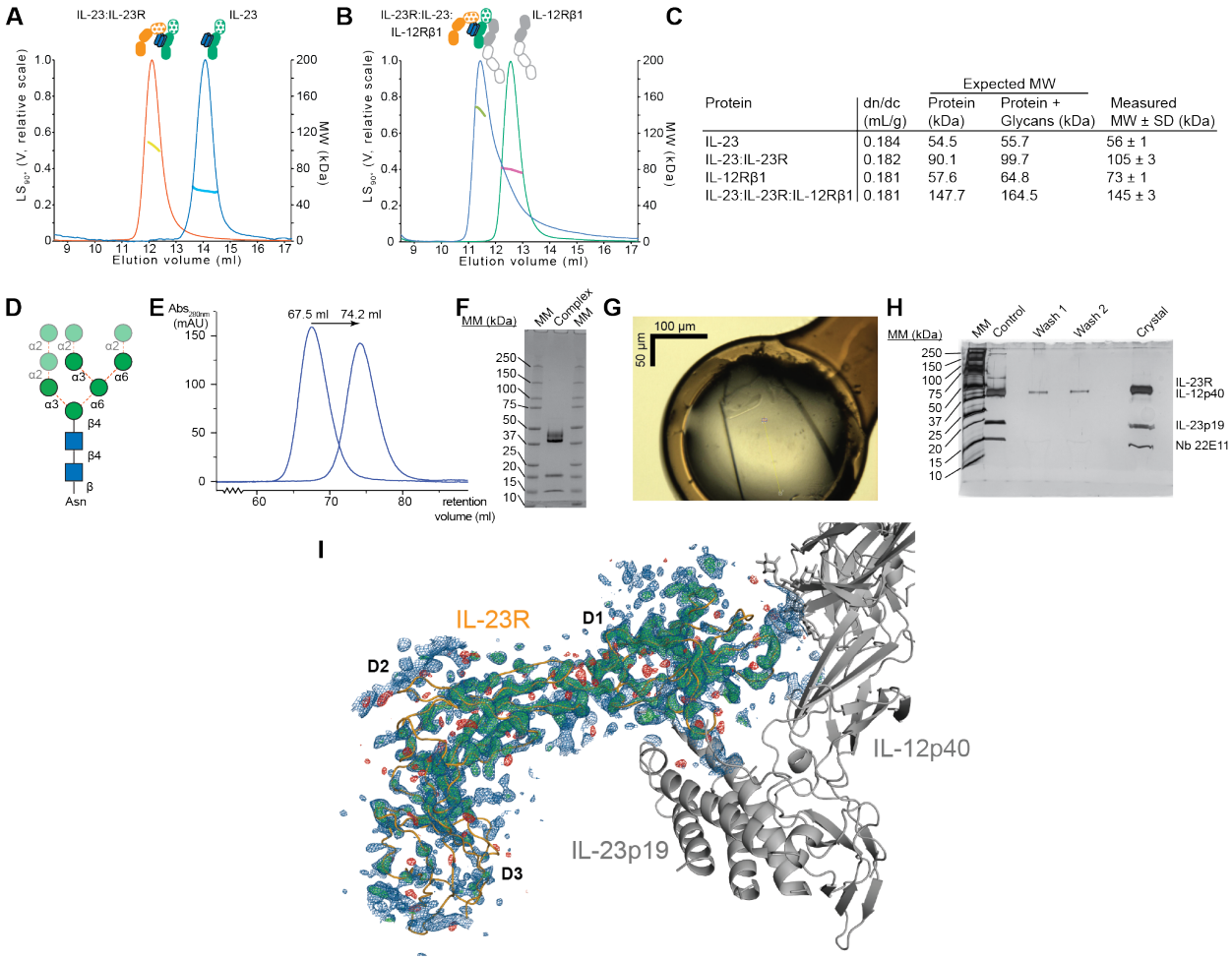

Protein	dn/dc (mL/g)	Expected MW Protein (kDa)	Expected MW Protein + Glycans (kDa)	Measured MW ± SD (kDa)
IL-23	0.184	54.5	55.7	56 ± 1
IL-23:IL-23R	0.182	90.1	99.7	105 ± 3
IL-12Rβ1	0.181	57.6	64.8	73 ± 1
IL-23:IL-23R:IL-12Rβ1	0.181	147.7	164.5	145 ± 3

Figure S2 (Related to Figure 1). Assembly and characterization of the IL-23:IL23R complex.
(**A**) Characterization of the IL-23 complex by SEC-MALLS. Elution profile recorded by the right-angle laser light scattering detector (left axis) plotted against determined molecular weight (right axis). IL-23 forms a binary complex with IL-23R. (**B**) The preformed IL-23:IL-23R can be further complemented with IL-12Rβ1 leading to a ternary complex. Molecular weights determined by MALLS are summarized in panel (**C**) Data are presented as average molecular weights ± standard deviations calculated in Excel over the selected region of the peaks. (**D**) Schematic representation of the N-linked glycans present in the IL-23:IL23R:Nb22E11 structure (Mannoses in green and GlcNAc in blue). Dashed orange lines represent bonds that could be hydrolyzed by Jack bean α-mannosidase. The α1-2 linked mannoses present at the non-reducing end of the oligosaccharide are normally removed by mannosidases in the Golgi during oligosaccharide maturation leading to a Man5GlcNAc2 oligosaccharides normally expected in HEK293S *MGAT1*$^{-/-}$ cells. (**E**) Trimming of the N-linked glycans on the IL-23:IL23R:Nb22E11 complex by Jack bean α-mannosidase leads to a clear increase in retention volume on a SD200 16/600 column. (**F**) Coomassie-stained SDS-PAGE analysis under reducing conditions of the IL-23:IL23R:Nb22E11 complex used for protein crystallization. IL-23R migrates as a fuzzy band just above IL-12p40 around 40 kDa. (**G**) Crystal of the IL-23:IL23R:Nb22E11 complex as mounted in a Dual thickness Microloop (MiTeGen, Ithaca, USA) for data collection at Petra III beamline P14 (EMBL-Hamburg, Germany) (**H**) Silver-stained reduced SDS-PAGE analysis of IL-23:IL23R:Nb22E11 crystals to characterize the molecular contents of the crystal. Starting from a crystallization drop, crystals were washed by serially transferring them to drops containing mother liquor (3 times). The first two wash drops were loaded in lanes Wash1 and Wash2. The final drop containing the crystals was loaded in the lane labelled Crystal. A crystallization droplet of the same protein complex that did not yield any crystals was loaded in the Control lane. IL-23R and IL-12p40 have similar electrophoretic patterns. Contaminants present in the original sample running around 65 kDa and 200 kDa are not present in the crystals. (**I**) Phasing of the IL-23:IL23R:Nb22E11 crystals by molecular replacement in Phaser using IL-23 and Nb22E11 as search models resulted in clearly interpretable difference density for IL-23R. Shown are mFo-DFc difference electron density maps calculated at +3 r.m.s.d. (green map) and -3 r.m.s.d. (red map), 2mFo-DFc map (blue map) calculated at +1.5 r.m.s.d.

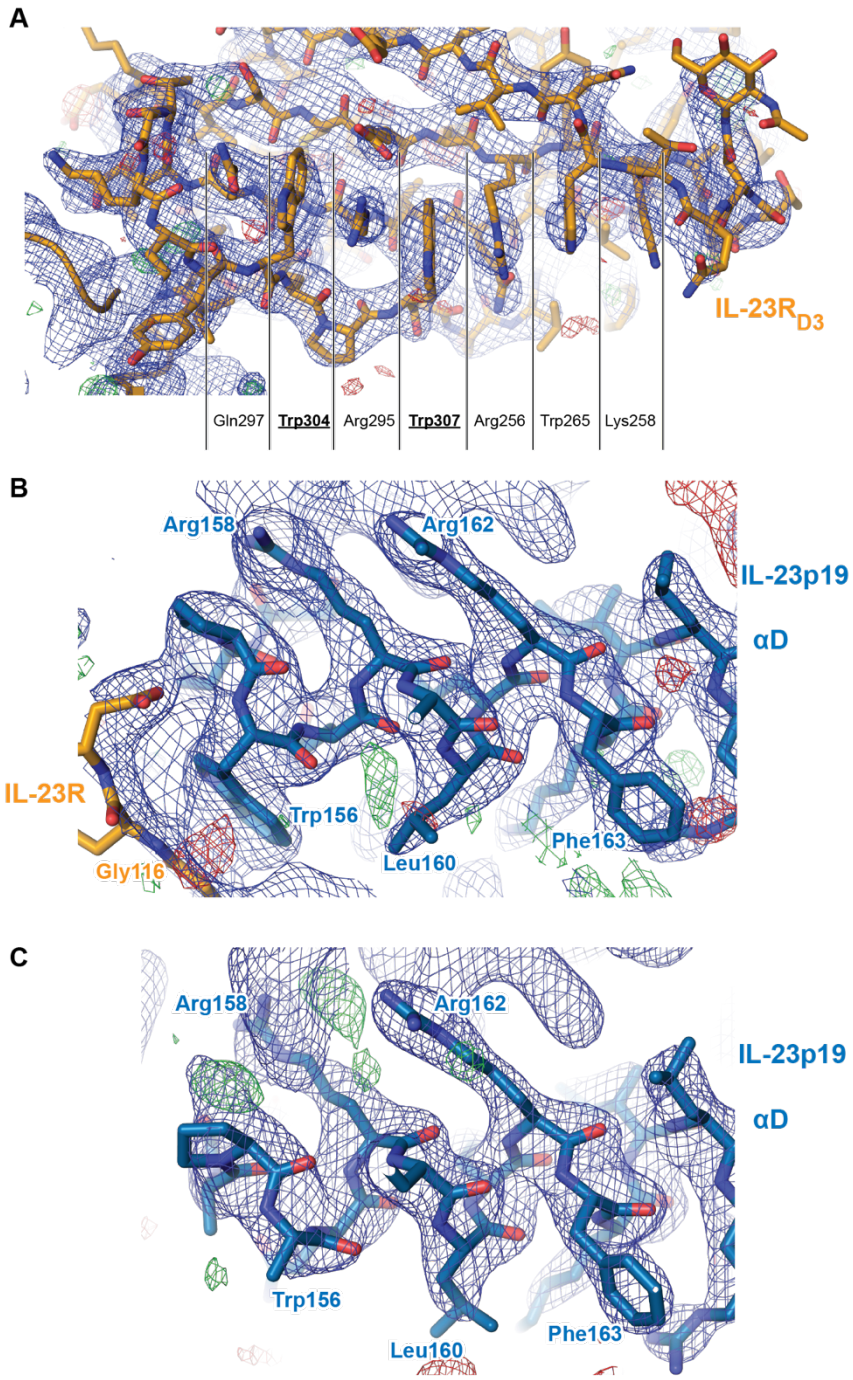

Figure S3 (Related to Results, Crystal structure of the human IL-23:IL-23R complex, Figure 1). Close-up views of regions of special interest in the IL-23:IL-23R complex

Electron density maps carved 5Å around the region of interest in Pymol. mFo-DFc map calculated at +3 r.m.s.d. (green map) and -3 r.m.s.d. (red map), 2mFo-DFc map (blue map) calculated at +1.5 r.m.s.d. The WSXWS motif on IL-23R domain 3 is part of an elaborate sidechain stacking arrangement running all along the side of the domain (**A**). The W residues part of the WSXWS motif are underlined and shown in bold. Electron density maps carved around the N-terminal part of IL-23p19 helix D in the IL-23:IL-23R:Nb22E11 (**B**) and unbound IL-23 (**C**) structures. The quality of the electron density around W156 is of remarkably better quality in the bound versus the unbound structure. There is no interpretable electron density present at the N-terminal part of helix D in support of a specific W156 sidechain rotamer. Which is indicative of inherent flexibility in this region.

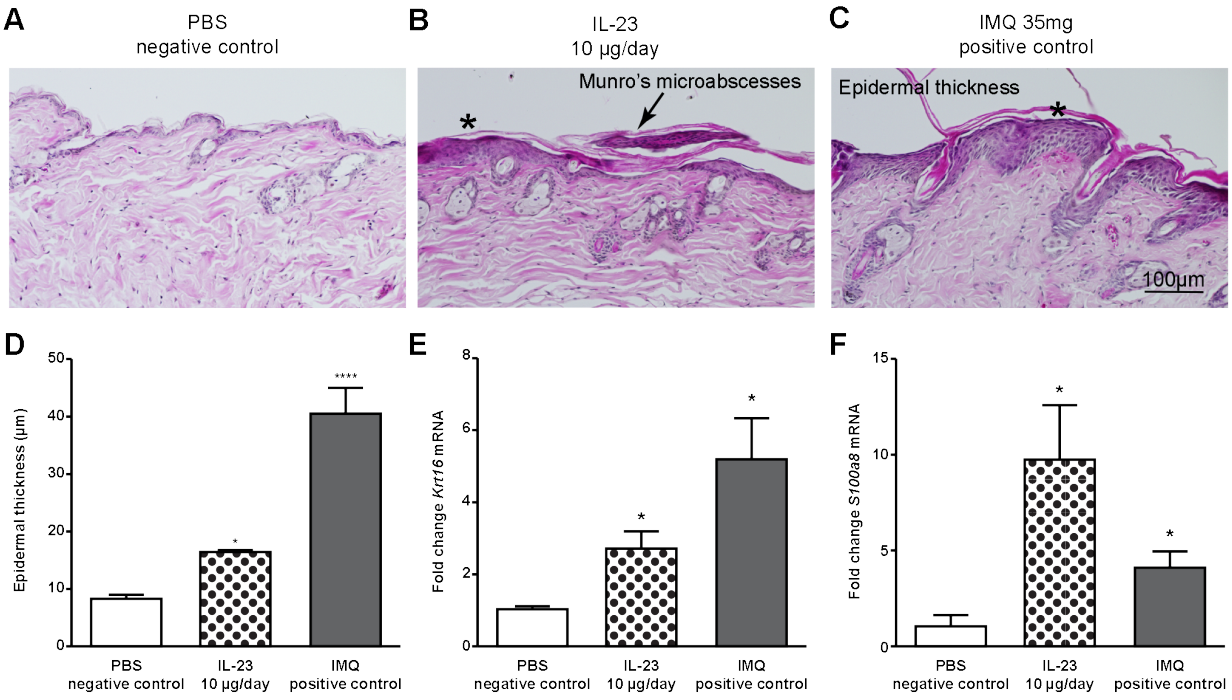

Figure S4 (Related to Figure 3). IL-23 dose validation and comparison with IMQ in induction of epidermal hyperplasia and markers of epidermal hyperplasia.

A-C. Representative H&E staining of cutaneous biopsies showing diffuse epidermal hyperplasia (acanthosis) (asterisk) with associated compact hyperkeratotic and parakeratosis of the stratum corneum and the formation of Munro's microabsecces (arrow), (scale bar 100 µm). **D.** Quantification of epidermal thickness by microscopy in the indicated mice treatments. Fold change in mRNA expression levels of *Krt16* **(E)** and *S100a8* **(F)** in IMQ and IL-23 WT treated skin compared with PBS injected skin assessed by qPCR at day 4. Data are presented as ± s.e.m, and p-values were determined using one-way ANOVA followed by Holm-Sidak's multiple comparisons test (*p < 0.05; **p < 0.01; ***p < 0.001; ****p < 0.0001). (*n*= 4 for each group).

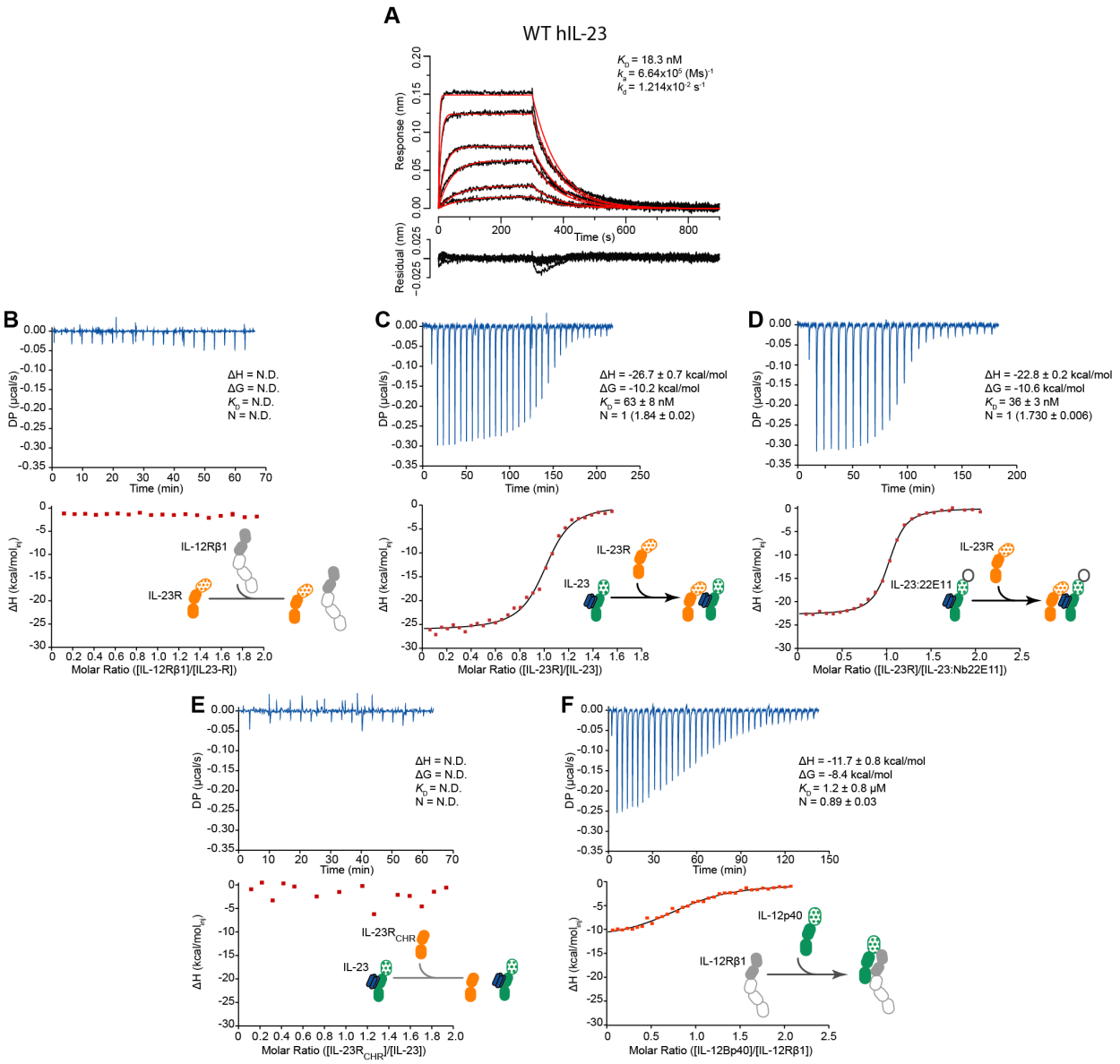

Figure S5 (Related to Figure 1, Figure 3 and Figure 4). Kinetic and thermodynamic characterization of interactions between various constructs/modules of IL-23, IL-23R, and IL-12Rβ1.

A) Representative BLI sensorgrams (black), fitted 1:1 model (red) and residual (black, bottom graph) used to characterize the binding kinetics (k_a, k_d) and affinity (K_D) of human IL-23 towards mouse IL-23R. Anti-human IgG Fc capture biosensors were coated with mIL-23R_Fc and dipped into a threefold dilution series of human cytokine (517 nM, 172 nm, 57 nM, 19 nM, 6 nM and 2 nM). (**C, D, F**) Representative ITC experiments performed on a VP-ITC machine or a PEAQ-ITC instrument (**B, E**). **B)** Titration of 102 μM IL-12Rβ1 in 10.2 μM IL-23R at 309.95 K. **C)** Titration of 70.2 μM IL-23R in 4.97 μM IL-23 at 310.15 K. **D**) Titration of 70.2 μM IL-23R in 4.0 μM IL-23 at 310.15 K. **E**) Titration of 60.0 μM IL-23R$_{CHR}$ in 6 μM IL-23 at 310.05 K **F**) Titration of 93.2 μM IL-12Bp40 in 8.8 μM IL-12Rβ1 at 310.15 K. The stoichiometry of experiments **C** and **D** were set to 1 and the concentration in the syringe was allowed to be fitted to account for binding incompetent IL-23R. The stoichiometry of the experiment before correction is reported between parenthesis. Fitted values are reported with their fitting errors as reported by the MicroCal PEAQ-ITC Analysis software version 1.1.0.1262.

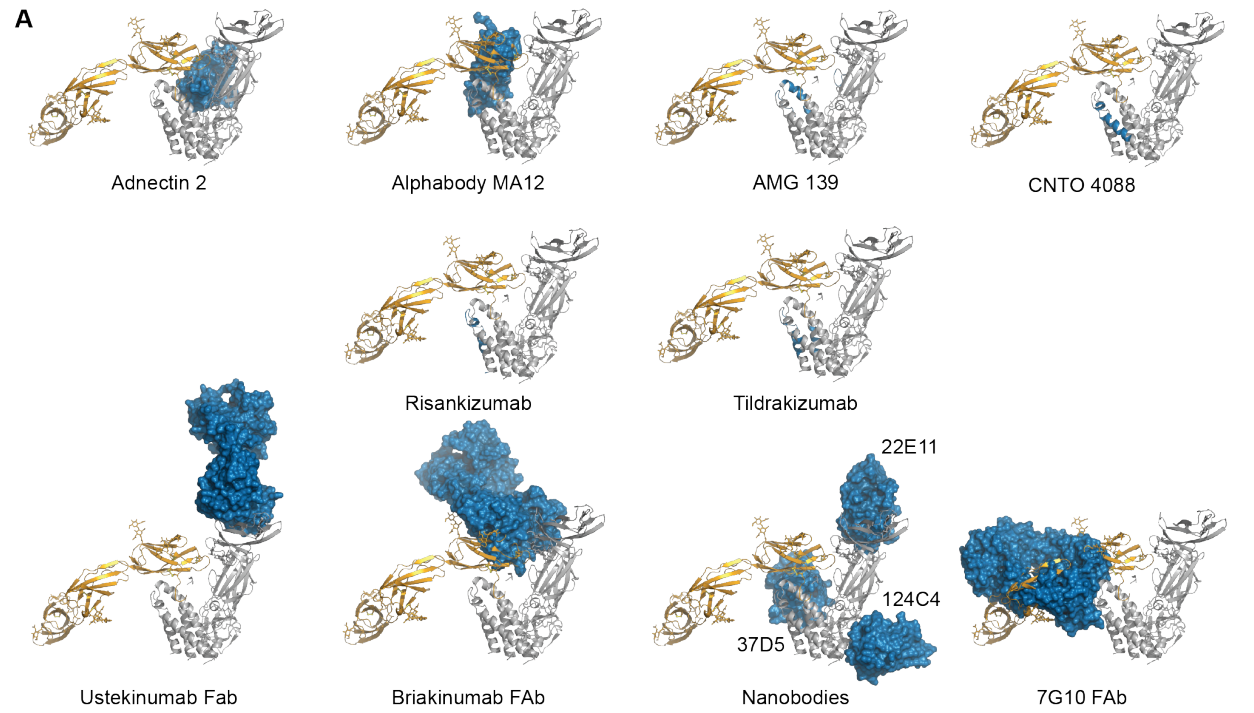

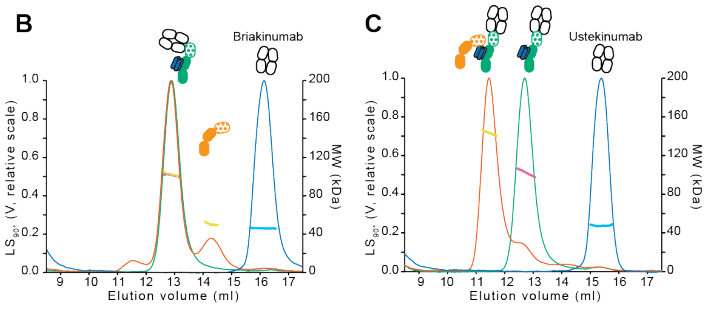

D

Protein	dn/dc (ml/g)	Expected MW: Protein (kDa)	Expected MW: Protein + Glycans (kDa)	Measured MW ± SD (kDa)
IL-23R*	0.178	35.6	44.0	50 ± 1
Briakinumab Fab	0.185	47.4	47.4	46.1 ± 0.2
IL-23:B Fab	0.185	101.9	103.1	101 ±1
IL-23:B Fab*	0.185	101.9	103.1	102 ± 1
Ustekinumab Fab	0.185	48.4	48.4	47.7 ± 0.5
IL-23:U Fab	0.184	102.9	104.1	102 ± 3
IL-23:IL-23R:U Fab	0.183	138.5	148.1	143 ±2

Figure S6 (Related to Figure 5 and Figure 6). Overview and structural mapping of IL-23 antagonists, and characterization by SEC-MALLS of IL-23:antibody complexes.

(**A**) Several IL-23 antagonists have been described in peer-reviewed literature as well as in patent literature. The structure of IL-23:IL-23R (in grey and orange respectively) is combined into a hybrid model with the structures of the IL-23 bound (IL-12 in case of ustekinumab) antagonist (in blue surface representation) when publically available. When no structure was publicly available the epitope described in the patents was mapped on the IL-23 structure and colored blue. The binding of most antagonists to IL-23 is incompatible with the binding of IL-23R. (**B,C**) Characterization of the binding of antibody Fabs to the preformed IL-23:IL23R complex in solution by SEC-MALLS. Elution profile recorded by the right-angle laser light scattering detector (left axis) plotted against determined molecular weight (right axis). Blue trace = Fab alone, green trace = IL-23:Fab complex, vermillion trace IL-23:IL-23R complex after addition of Fab (**B**) Briakinumab Fab competes with IL-23R for IL-23 leading to IL-23:Fab and unbound IL-23R (vermillion trace). (**C**) Ustekinumab Fab binds distally of the IL-23:IL-23R interaction site thereby forming a ternary IL-23:IL23R:Fab complex. Molecular weights determined by MALLS are summarized in panel (**D**) Values with an asterisc are calculated from the experiment where briakinumab Fab was added to the IL-23:IL-23R complex. Data are presented as average molecular weights ± standard deviations calculated in Microsoft Excel over the selected region of the peaks.